JOURNAL OF MATERIALS SCIENCE 14 (1979) 1657–1661

Fracture of a brittle particulate composite

Part 2 *Theoretical aspects*

DAVID J. GREEN
Ceramic Section, Mineral Sciences Laboratories, Canada Centre for Mineral and Energy Technology, Department of Energy, Mines and Resources, Ottawa, Ontario, Canada

PATRICK S. NICHOLSON, J. DAVID EMBURY
Department of Metallurgy and Materials Sciences, McMaster University, Hamilton, Ontario, Canada

Previous models for crack–particle interactions in brittle composites are modified to account for penetrable obstacles, obstacle shape and secondary crack interactions. The modified model is applied to a glass-unbonded nickel sphere composite system, the experimental aspects of which were summarized in Part 1. Increases in fracture energy are explained in terms of local crack blunting. It is shown that these results fall, as expected, between those for an entirely sharp crack front and an entirely blunt one.

1. Introduction

In Part 1 [1] it was shown that ultrasonic fractography could be used to observe the interactions between a crack front and second phase particles in a brittle composite. It was also shown that the fracture surface energy of a glass–nickel composite increased as the volume fraction of nickel increased. In this system the obstacles were non-bonded.

The interaction of a crack front with impenetrable obstacles has been discussed theoretically by Evans [2]. It was found, however, that the increase in toughness for the glass–nickel system was much less than predicted. There is clearly a need, therefore, to extend the model to cover the interaction of a crack front with weaker obstacles.

2. The microscopic crack bowing stress

For crack–particle interaction to provide a useful toughening mechanism, it is important to assess the magnitude of the local stress needed to change the crack shape as it by-passes the obstacle on a microscopic level. The unit step will be the bowing of the crack between a pair of obstacles. In practice, a segment of crack front, bowing between a pair of obstacles will be influenced by neighbouring segments and this effect should also be included in the calculations. Provided the crack front moves so as to intersect the obstacles in a particulate system, the maximum interaction will occur where the particles can be considered "impenetrable". The stress then needed to circumvent the obstacles will be independent of their character. In systems where the obstacles are weaker, the particle or the particle–matrix interface may fail before the crack-bowing process is complete. It should be noted that circumvention of an impenetrable obstacle by crack bowing leaves the obstacles as ligaments behind the crack front to still resist crack opening.

2.1. The motion of secondary cracks

Consider the extension of a through-the-thickness surface crack of length $2C'$, impeded by a pair of rectangular obstacles† in its path (Fig. 1). The stress (σ_s) needed to extend a semi-circular crack of diameter $2C$ between the obstacles can be evaluated by considering the motion of the secondary crack in the stress field of the primary

† For the initial calculation, the cross-sections of the obstacles is assumed to be rectangular so that the spacing between the particles does not change during the bowing process.

0022–2461/79/071657–05 $2.50/0

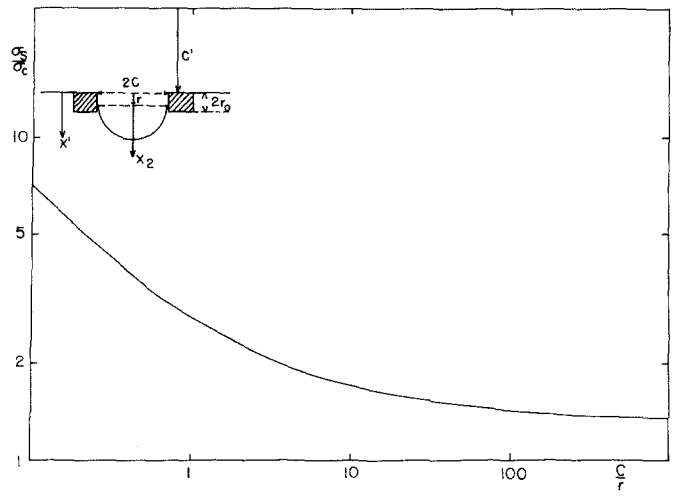

Figure 1 Stress to move semicircular secondary crack between the rectangular obstacles.

crack [2]. For this calculation it is assumed that C' is much greater than C (in Fig. 1).

The stresses ahead of the primary crack and orthogonal to the crack plane (σ_{11}) are [3]:

$$\sigma_{11} = \sigma_s \left(1 + \frac{C'}{2X'}\right)^{1/2} \quad (1)$$

where X' is the distance from the crack tip. This equation is valid in the elastic region ahead of the plastic zone provided X' is very much larger than the crack tip radius [4].

Unimpeded extension of the secondary crack will occur when it reaches its maximum stress position. This is related to the obstacle strength (r). Here r will be defined in terms of the distances that the origin of the semi-circular crack has moved from the primary crack front. For impenetrable obstacles this was assumed to occur when $r = 2r_0$ [2]. For weaker obstacles $r < 2r_0$. In the following calculation such assumptions are unnecessary as the obstacle strength treated is a variable parameter.

The stresses applied to the crack at breakaway are (from Equation 1).†

$$\sigma_{11} = \sigma_s \left(1 + \frac{C'}{2r + 2X_2}\right)^{1/2}, \quad (2)$$

provided that the obstacles are much larger than the plastic zone size. X_2 is a co-ordinate located at the secondary crack origin (Fig. 1). Following Evans [2], it is possible to calculate σ_s in terms of the stress (σ_c) needed to move the primary crack in the absence of any obstacles. Using a computer to carry out the numerical integrations, the resulting stress ratio σ_s/σ_c, is given in Fig. 1 in terms of the secondary crack size and the obstacle strength. For large C/r values, the asymptotic value of σ_s/σ_c was determined to be 1.30 [5].

The secondary crack may not be semi-circular at the maximum stress position and this analysis attempts to correct this by assuming that the crack be semi-elliptical. The stress now needed is that to move a semi-elliptical secondary crack, and the transformation is undertaken by determining the stress to move a semi-circular crack of equivalent depth (a) to the semi-elliptical crack, assuming that the applied tensile stress on both these secondary cracks is uniform. The analytical procedure requires calculation of the crack shape at breakaway $(a/2C)^*$ for the semi-elliptical crack, followed by calculation of σ_E/σ_S.

Using computer techniques, values of $(a/2C)^*$ and σ_E/σ_C were calculated (Figs. 2 and 3). Fig. 2

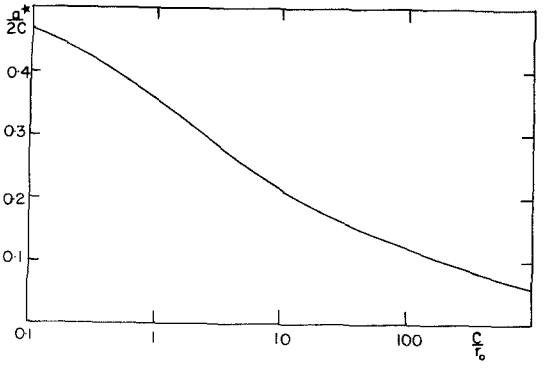

Figure 2 Crack shape at breakaway.

† This equation differs slightly from that of the original calculation for impenetrable obstacles [2] where $r = 2r_0$. This discrepancy leads to a difference between the values of σ_s as calculated here to those in the original calculation.

indicates that, for impenetrable obstacles at high volume fractions, the crack shape at breakaway tends to be semi-circular while for low volume fractions or weak obstacles the crack front will tend to remain straight. Predicted values of $(a/2C)^* > 0.5$ [2] were not found in the current work. Fig. 2 allows prediction of the crack shape provided r_0 is known. This information can be compared with the ultrasonic fractography data (Part 1). Fig. 3 indicates that, at low volume fraction or for weak obstacles, $\sigma_E \simeq \sigma_c$. For stronger obstacles at higher volume fractions $\sigma_E > \sigma_c$. Hence the motion of a crack between a pair of obstacles can contribute to the fracture surface energy of a composite. In this case the prediction can be used for comparison with experimentally determined values as;

$$\left(\frac{\sigma_E}{\sigma_c}\right)^2 = \frac{E_c\Gamma_c}{E_0\Gamma_0}. \quad (3)$$

This calculation indicates that, once the equilibrium crack front shape is attained, it moves past the obstacles and σ_E/σ_c increases. For impenetrable obstacles the maximum stress position will occur when $r = 2r_0$. The maximum stress position could, however, occur before this position for: (a) the obstacle may fail; (b) the obstacle spacing may not be constant (non-rectangular obstacles); or (c) interactions between neighbouring crack segments may influence the bowing process.

2.2. Obstacle shape and crack interactions

For non-rectangular impenetrable obstances σ_E/σ_c values can be determined from Fig. 3, provided the actual value of the major axis of the semi-ellipse can be calculated for various r values. For circular obstacles (radius r_0), an example is given in Fig. 4 for $C/r_0 = 1$. Repeating for various C/r_0 values gives the corrected values of σ_E/σ_c (σ'_E/σ_c) and the maximum stress position (r'). These results are shown in Table I wherein it is clear that, even for impenetrable obstacles, the maximum stress position is at $r < 2r_0$.

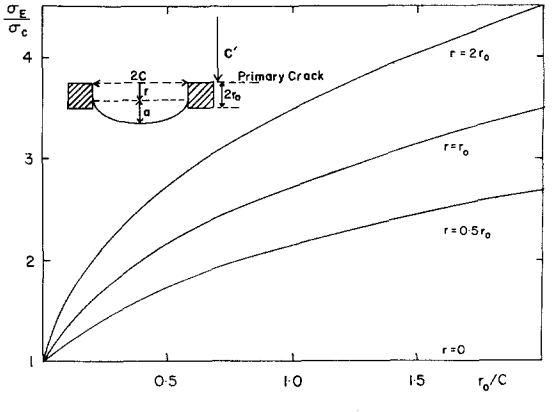

Figure 3 Stress to move semi-elliptical secondary crack between two rectangular obstacles for different breakaway positions

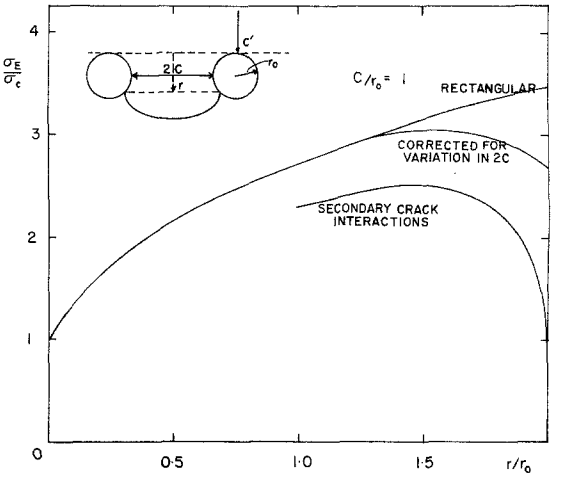

Figure 4 Stress to move semi-elliptical secondary crack between two impenetrable circular obstacles with corrections for particle shape and secondary crack interactions $(C/r_0 = 1)$.

Interaction between neighbouring crack segments can also be determined, provided they are assumed co-planar. The value of σ'_E is reduced further by this interaction (σ''_E). σ''_E can be determined from the solution for a linear array of equally spaced, co-planar cracks of length $2C$ [6]:

$$\frac{\sigma''_E}{\sigma'_E} = \left[\frac{\pi}{2(1 + W/C)}\right]^{1/2}\left(\tan\left[\frac{\pi}{2(1 + W/C)}\right]\right)^{1/2}, \quad (4)$$

TABLE I

$\frac{r_0}{C}$	$\frac{\sigma_E\dagger}{\sigma_C}$	$\frac{\sigma_E\dagger}{\sigma_C}$	$\frac{r'}{r_0}$	$\frac{\sigma''_E}{\sigma_C}$	$\frac{r''}{r_0}$
0.10	1.61	–	–	–	–
0.25	2.16	2.02	1.8	1.19	1.4
0.50	2.72	2.52	1.8	1.80	1.4
1.00	3.48	3.05	1.6	2.52	1.4
1.25	3.81	3.25	1.5	2.86	1.4
2.00	4.52	3.75	1.3	3.52	1.3
2.50	4.96	4.08	1.2	3.95	1.2
5.00	7.02	–	–	–	–

†For the case $r = 2r_0$.

where W is the distance between the co-planar cracks. For circular obstacles the value of W can be determined geometrically in terms of r_0 for each stage of the bowing process assuming the obstacles do not fail. Values of σ''_E/σ_C as a function of r are shown in Fig. 4 for $C/r_0 = 1$. This interaction reduces the maximum stress position to a lower values of $r(r'')$. Repeating this procedure for several values of C/r_0 gave the σ''_E/σ_C and r'' values listed in Table I. The various refinements to σ_E/σ_C and r are summarized in Fig. 5 as a function of r_0/C.

In the case of obstacle failure, the critical value of r must be determined theoretically or experimentally before σ_E/σ_C can be calculated.

2.3. Limitations of the present approach

The model assumes that the secondary cracks are semi-elliptical and co-planar. This latter assumption was made to account for interactions between neighbouring secondary cracks. In the composites studied however, the neighbouring segments are seldom co-planar and a fracture surface step forms at the rear of the particle (Part 1). The analysis also ignores strain fields associated with the particles. These can arise as a result of self-stresses or elastic modulus interactions [7]. These strain fields will influence the stress on the crack front during its approach and its bowing. Furthermore, above a certain volume fraction these strain fields will overlap. From Fig. 5 it is clear that above $r_0/C = 1$ the overlap of the strain fields will be significant. For example, if $2C$ was equated to the nearest-neighbour edge-to-edge distance for a random array of monosized, dispersed spheres [8], values of $r_0/C \geqslant 1$ occur at volume fractions above $\simeq 0.06$. The closeness of the particles will also interfere with the bowing of the secondary cracks. The values of σ_E/σ_C will be further reduced for values of $r_0/C > 1$. The experimental data of Part 1 show the fracture surface energy reaches a maximum between 0.10 and 0.20 volume fraction. This may result from the overlap of the particle strain fields. It has also been proposed that the strain on the obstacle will increase as r_0/C increases [9]. This will increase the possibility of obstacle penetration with increasing r_0/C, also reducing σ_E/σ_C.

3. Crack-front interaction with non-bonded obstacles or pores

The fracture surface energy data from the glass–nickel system (Part 1) is included in Fig. 5. The data points are lower than those predicted for circular obstacles. If crack interactions are considered, the agreement is improved but this refinement is questionable as fracture surface steps are formed behind the particles in this system (Part 1). A further problem is that the ultrasonic fractographs clearly show the bowing crack segments are not semi-elliptical and the primary crack front is not pinned at the front of the obstacle as envisaged in the model. Similar ultrasonic data were also found for a glass–pore system [10]. It is clear, however, that the nickel spheres and pores impede the motion of the crack and, for the glass–nickel system, this leads to an increase in the fracture surface energy.

For interaction with non-bonded obstacles or pores it was postulated that the resistance to crack motion is a result of localized crack blunting leading to local relaxation of the stress field ahead of the primary crack. The stresses ahead of a primary crack (tip radius, ρ) is [11];

$$\sigma_{11} = 2\sigma_s\left(\frac{C'}{\rho + 4X'}\right)^{1/2}. \quad (5)$$

Comparing this with Equation 2, shows that ρ plays a similar role to the r of the initial calcu-

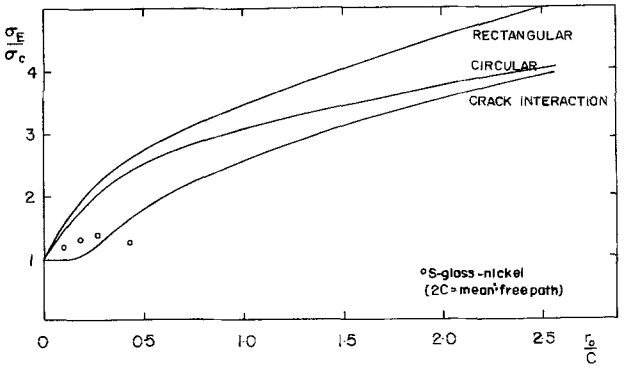

Figure 5 Summary of refinements to σ_E/σ_C and comparison to experimental data on S-glass–nickel system.

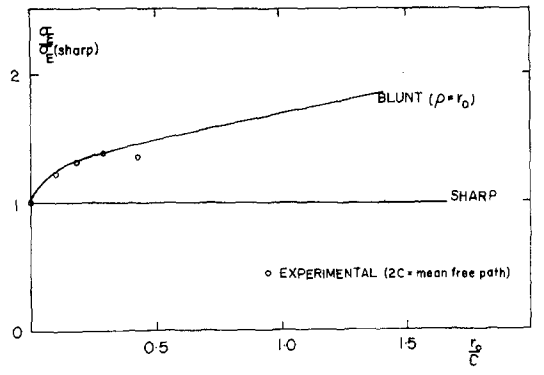

Figure 6 Theoretically predicted values of σ_E for blunted ($\rho = r_0$) and sharp primary cracks for comparison with experimental data on S-glass–nickel system.

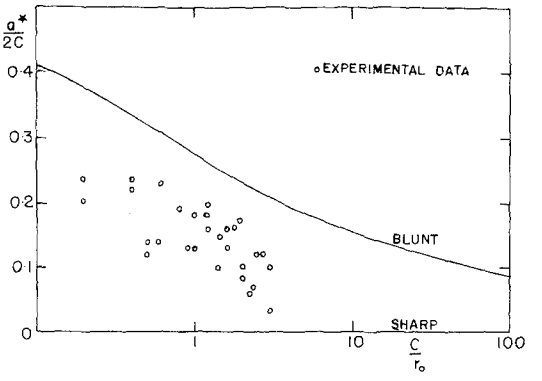

Figure 7 Experimental data on crack-shape-at-breakaway determined from ultrasonic fractography in comparison with that expected for an entirely blunt and an entirely sharp crack front.

lations. Unfortunately, ρ will vary along the length of the primary crack front from a maximum of r_0 at the middle of the obstacle to atomic dimensions between the obstacles. It is possible, however, to repeat the analysis for the two extreme cases, i.e. $\rho = r_0$ and $\rho \to 0$. For the latter case, the earlier work indicated $\sigma_E/\sigma_C \simeq 1$. The results of these analyses (without correction for particle shape and crack interactions) are shown in Fig. 6. The experimental data (Part 1) lies between the two extreme cases. The crack shape at breakaway was determined from the ultrasonic fractography for comparison with theory. These results are given in Fig. 7. The experimental data lie between the two extreme cases.

Acknowledgement

The authors would like to express their thanks to Colin Sargent for his help setting up the computer programmes.

References

1. D. J. GREEN, P. S. NICHOLSON and J. D. EMBURY, *J. Mater. Sci.* 14 (1979) 1413.
2. A. G. EVANS, *Phil. Mag.* 26 (1972) 1327.
3. I. N. SNEDDON, *Proc. Roy. Soc.* A187 (1946) 229.
4. A. S. TETELMAN and A. J. MCEVILY, Jr. "Fracture of Structural Materials" (Wiley, New York, 1967) p. 49.
5. D. J. GREEN, Ph.D. Thesis, McMaster University (1977).
6. P. C. PARIS and G. C. SIH, ASTM Spec. Tech. Publ., no. 381 (1967) p. 30.
7. D. J. GREEN and P. S. NICHOLSON, "Fracture Mechanics of Ceramics", Volume 4, edited by R. C. Bradt, D. P. H. Hasselman and F. F. Lange (Plenum, New York, 1978) p. 945.
8. P. B. BANSAL and A. J. ARDEL, *Metallogr.* 5 (1972) 97.
9. A. G. EVANS and L. J. GRAHAM, *Acta Met.* 23 (1975) 1313.
10. D. J. GREEN, P. S. NICHOLSON and J. D. EMBURY, *J. Mater. Sci.* 12 (1977) 987.
11. V. WEISS, ASME Paper no. 62 WA-270 (1962).

Received 22 August and accepted 9 October 1978.